

CAV2009 Paper No. 73

LARGE EDDY SIMULATION OF CAVITATION INCEPTION IN A HIGH SPEED FLOW OVER AN OPEN CAVITY

Ehsan Shams and Sourabh V. Apte*

Computational Flow Physics Laboratory

School of Mechanical Industrial and Manufacturing Engineering

Oregon State University, 204 Rogers Hall, Corvallis, OR 97331

Email: sva@enr.orst.edu

ABSTRACT

Large-eddy simulation of flow over an open cavity corresponding to the experimental setup of Liu and Katz [1] is performed. The flow Reynolds number based on the cavity length and the free stream velocity is 170,000. The filtered, incompressible Navier-Stokes equations are solved using a co-located grid finite-volume solver with the dynamic Smagorinsky model for subgrid scale closure. The computational grid consists of around five million grid points with two million points clustered around the shear layer and the wall-layer over the leading edge is resolved. The only input from the experimental data is the mean velocity profile at the inlet condition. The mean flow is superimposed with turbulent velocity fluctuations generated by solving a forced periodic duct flow at free-stream Reynolds number. The flow statistics, including mean and rms velocity fields and pressure coefficients, are compared with the experimental data to show reasonable agreement. Cavitation inception is investigated using two approaches: (i) a discrete bubble model wherein the bubble dynamics is computed by solving the Rayleigh-Plesset and the bubble motion equations using an adaptive time-stepping procedure, and (ii) a scalar transport model for the liquid volume fraction with source and sink terms for phase change. The cavitation inception occurs near the trailing edge similar to that observed in the experiments. A periodic growth and decay of bubble size and liquid vapor fraction is observed above the trailing edge owing to local variations in pressure minima. The dynamic interactions between traveling vortices in the shear layer

and the trailing edge affect the value and location of the pressure minima.

1 INTRODUCTION

The problem of cavitation has been widely studied owing to its influence on structural vibrations, noise production, erosion of propulsor blades, among others [2]. To devise strategies avoiding cavitation, it is necessary to predict its inception in unsteady turbulent flows. Rood [3] provides a review of different mechanisms of cavitation inception emphasizing that cavitation inception and turbulence are inseparable in many applications. Therefore, predictive numerical approaches (such as large-eddy simulations) for turbulent flows in complex flow configurations are necessary to accurately capture the inception process. However, modeling cavitation inception and its unsteady evolution in engineering geometries is a challenging task. Liu and Katz [1] (henceforth referred to as LK2008) designed a well quantified experiment on high speed flow over an open cavity which can be used for detailed validation of the numerical approach in predicting cavitating flows in complex geometries as well as development and testing of subgrid scale models.

The cavitation number [$\sigma_i = (P_{ref} - P_v)/(0.5\rho U_\infty^2)$], where P_v is the vapor pressure, ρ is fluid density, U_∞ is reference velocity, and P_{ref} is reference pressure value at which cavitation occurs, has typically been used to predict cavitation inception. If we assume that inception occurs when the pressure drops below vapor pressure, then a critical coefficient of pressure can be defined as $C_{p,min} = (P_{min} - P_{ref})/(0.5\rho U_\infty^2) = -\sigma_i$, where P_{min} is the minimum pressure within the domain. In turbulent flows, the

* Address all correspondence to this author.

location and the value of minimum pressure can change dramatically, and thus can affect the inception process. For high-speed flow over an open cavity LK2008 showed that cavitation inception occurs above the trailing edge. However, they also observed a periodic variation in the amount of cavitation due to variations in pressure fields induced by the turbulent shear flow above the cavity.

Several numerical studies on cavitation inception have been performed for gaseous cavitation (i.e. growth of air micro-bubbles without significant transfer of mass from liquid to the bubble) [4–11]. A majority of these studies used Reynolds-averaged Navier Stokes (RANS) models to predict cavitation inception. Recently, large-eddy simulation (LES) has also been used to study cavitation inception in a flow over a square cylinder [12]. A simple algebraic criterion for inception was developed based on stability of bubble nuclei to show good predictive capability of the LES methodology.

In the present work, LES of turbulent shear flow developing past an open cavity is performed to first investigate the predictive capability of LES with the dynamic Smagorinsky model [13]. Distribution of the coefficient of pressure (mean and *rms*) is used to identify cavitation inception regions over the trailing edge of the cavity and inside the shear layer. Cavitation inception is also studied by considering two types of models: (i) a discrete-bubble model (DBM) for gaseous cavitation based on the bubble-dynamics represented by Rayleigh-Plesset equation, and (ii) a scalar-transport model typically used for vaporous cavitation (involving phase change) [14, 15]. As the first step, the effect of the gaseous or vapor bubble dynamics on the fluid are neglected; that is the bubbles are assumed not to significantly affect the flow.

In the following sections, a brief overview of the mathematical formulation for the two models is presented. The discrete bubble model, involves computation and tracking of large number bubble nuclei and can be expensive. An adaptive time-stepping scheme is developed and validated for efficient computation. These models are coupled with an LES solver and the results obtained are discussed in detail.

2 MATHEMATICAL FORMULATION

In this section, the mathematical formulation for the single-phase LES and the two-phase flow models are described. The three-dimensional, incompressible, filtered Navier-Stokes equations are written as

$$\frac{\partial \bar{u}_i}{\partial x_i} = 0 \quad (1)$$

$$\frac{\partial \bar{u}_i}{\partial t} + \frac{\partial \bar{u}_i \bar{u}_j}{\partial x_j} = -\frac{1}{\rho_\ell} \frac{\partial \bar{P}_\ell}{\partial x_i} + \nu_\ell \frac{\partial^2 \bar{u}_i}{\partial x_j \partial x_j} - \frac{\partial \tau_{ij}^r}{\partial x_j}, \quad (2)$$

where τ_{ij}^r denotes the anisotropic part of the subgrid-scale stress tensor, $u_i u_j - \bar{u}_i \bar{u}_j$, and the overbar indicates filtered variables, ν_ℓ

is the kinematic viscosity and ρ_ℓ is the density of the liquid. The dynamic Smagorinsky model [13] is used for τ_{ij}^r .

2.1 Discrete Bubble Model

The discrete-bubble model is based on an Eulerian-Lagrangian approach. A continuum description is used for the liquid phase with discrete Lagrangian tracking of the bubbles. The bubbles are usually treated as spherical point-particles with models for fluid-bubble interaction forces and bubble-bubble interactions. The bubble growth and collapse is modeled using the Rayleigh-Plesset equation [6, 11, 16]. Typically, in this type of discrete bubble model, small-size nuclei are assumed trapped inside the fluid. Existing nuclei or microbubbles may contain gas or vapor or a mixture of both. These nuclei may undergo rapid changes in size due to local pressure variations and can be used as an indicator of cavitation inception. The growth and collapse of bubbles can affect the fluid flow through momentum coupling as well as through changes in bubble volume; that is through variations in local bubble and liquid volume fractions (Θ_b , Θ_ℓ) defined as:

$$\Theta_b(\mathbf{x}_{cv}) = \sum_{b=1}^{N_b} V_b \mathcal{G}_\Delta(\mathbf{x}_{cv}, \mathbf{x}_b); \quad \Theta_\ell = 1 - \Theta_b \quad (3)$$

where \mathcal{G}_Δ is the interpolation function, N_b is the total number of bubbles, and the summation is over all bubbles. These changes in local void fractions can alter the fluid flow and pressure distributions by creating a non-zero velocity divergence:

$$\nabla \cdot \mathbf{u} = -\frac{1}{\rho_\ell \Theta_\ell} \frac{D}{Dt} (\rho_\ell \Theta_\ell) \quad (4)$$

where $\frac{D}{Dt}$ is the material derivative with respect to fluid velocity. A mixture-theory based DBM model accounting for void fraction variations has been developed [17, 18]. In the present work we focus on cavitation inception, and do not consider the bubble-fluid coupling as well as effects of local void fraction variations. The bubbles are thus simply tracked by solving the following equations for the position (\mathbf{x}_b), velocity (\mathbf{u}_b), and bubble radius (R_b):

$$\frac{d}{dt}(\mathbf{x}_b) = \mathbf{u}_b \quad (5)$$

$$m_b \frac{d}{dt}(\mathbf{u}_b) = \sum \mathbf{F}_b \quad (6)$$

$$\rho_\ell \left[R_b \frac{d^2 R_b}{dt^2} + \frac{3}{2} \left(\frac{dR_b}{dt} \right)^2 \right] = P_b - \bar{P}_{out} - \frac{2\sigma}{R_b} - \frac{4\mu_\ell}{R_b} \frac{dR_b}{dt} \quad (7)$$

where m_b is the mass, $\sum \mathbf{F}_b$ is the total force acting on the bubble, P_b and \bar{P}_{out} are the pressures inside and outside of the bubble, σ

is the surface tension coefficient, and μ_ℓ and ρ_ℓ are the liquid viscosity and densities, respectively. To estimate P_b , it is typically assumed that the bubble contains some contaminant gas which expands or contracts according to adiabatic or isothermal processes [19, 20]. The bubble inside pressure consists of contribution from the gas pressure (P_g) and the vapor pressure (P_v). The gas-pressure is computed as:

$$P_b = P_v + P_g = P_v + P_{g,0} \left(\frac{R_{b,0}}{R_b} \right)^{3\eta}, \quad (8)$$

where $P_{g,0}$ and $R_{b,0}$ are the reference partial pressure and bubble radius, respectively. For isothermal bubble expansion $\eta = 1$ whereas for an adiabatic expansion, $\eta = c_p/c_v$ (the ratio of specific heats of the gas at constant pressure and volume). The outside pressure \bar{P}_{out} is taken as the pressure field interpolated to the bubble center location. Chahine and co-workers [5, 6] have shown that bubble surface-averaged pressure (SAP) provides a better representation of the outside pressure. The net force acting on each individual bubble is given as [4]:

$$\sum \mathbf{F}_b = \mathbf{F}_G + \mathbf{F}_P + \mathbf{F}_D + \mathbf{F}_L + \mathbf{F}_{AM} + \mathbf{F}_{coll} + \mathbf{F}_{R_b} \quad (9)$$

where $\mathbf{F}_G = (\rho_b - \rho_\ell)V_b\mathbf{g}$ is the gravitational force, $\mathbf{F}_P = -V_b\nabla P$ is the pressure force due to far-field pressure gradients, $\mathbf{F}_D = -\frac{1}{2}C_D\rho_\ell\pi R_b^2|\mathbf{u}_b - \mathbf{u}_\ell|(\mathbf{u}_b - \mathbf{u}_\ell)$ is the drag force, $\mathbf{F}_L = -C_L\rho_\ell V_b(\mathbf{u}_b - \mathbf{u}_\ell) \times \nabla \times \mathbf{u}_\ell$ is the lift force, $\mathbf{F}_{AM} = -\frac{1}{2}\rho_\ell V_b \left(\frac{D\mathbf{u}_b}{Dt} - \frac{D\mathbf{u}_\ell}{Dt} \right)$ is the added mass force, and \mathbf{F}_{coll} is the inter-bubble or bubble-wall collision forces. The force $\mathbf{F}_{R_b} = -4\rho_\ell\pi R_b^2(\mathbf{u}_b - \mathbf{u}_\ell) \frac{dR_b}{dt}$ represents momentum transfer due to variations in bubble size. Here, V_b and R_b are the bubble volume and radius, the subscripts 'b' and 'g' correspond to the bubble and the fluid, respectively. Inter-bubble and bubble-wall interaction forces are computed using the standard collision models typically used in the discrete element method [18]. Several different models for the drag (C_D) and lift (C_L) coefficients have been proposed that account for bubble deformation and variations in bubble Reynolds numbers ($Re_b = \rho_\ell|\mathbf{u}_b - \mathbf{u}_\ell|2R_b/\mu_\ell$) [21]. The drag coefficient used in this study is given as:

$$C_D = \frac{16}{Re_b} (1 + 0.15Re_b^{0.687}).$$

The bubble dynamics is mainly governed by the outside pressure changes. In low pressure regions, the bubble size can vary rapidly and the Rayleigh-Plesset equations become very stiff. An adaptive time stepping algorithm is needed to efficiently solve for several bubble trajectories and still keep the overall computational time small [17].

2.2 Scalar Transport Model

Eulerian-Eulerian two-phase models are also commonly employed in cavitation studies [14, 15, 22, 23]. These models usually are important for vaporous-cavitation where a large region of the fluid phase consists of a compressible vapor cavity. These models involve actual phase transition in regions where the local pressure drops below the vapor pressure. A scalar transport equation is solved for the conservation of liquid volume fraction (Θ_ℓ). The creation and destruction of the liquid mass is modeled through source and sink terms in the scalar transport model:

$$\frac{\partial \Theta_\ell}{\partial t} + \nabla \cdot (\Theta_\ell \bar{\mathbf{u}}) = \dot{m}^+ + \dot{m}^-, \quad (10)$$

where the source terms \dot{m}^- and \dot{m}^+ represent the destruction (evaporation) and production (condensation) of the liquid. They are both functions of the local and vapor pressures:

$$\dot{m}^- = \frac{C_{dest}\rho_\ell \min(P_\ell - P_v, 0)\Theta_\ell}{\rho_v(0.5\rho_L U_\infty^2)t_\infty} \quad (11)$$

$$\dot{m}^+ = \frac{C_{prod} \max(P_\ell - P_v, 0)(1 - \Theta_\ell)}{(0.5\rho_\ell U_\infty^2)t_\infty}, \quad (12)$$

where C_{dest} and C_{prod} represent the empirical constants and t_∞ is the characteristic time-scale associated with the flow. In this work, C_{dest} and C_{prod} are set to 1.0 and 80, respectively, based on similar values used by Senocak & Shyy [24]. The time scale is set equal to the flow-through time based on the cavity length (L) and the mean flow velocity in the duct (U_∞).

The production of the vapor leads to local changes in the mixture density, $\rho_m = \rho_\ell\Theta_\ell + \rho_v(1 - \Theta_\ell)$ where ρ_v is the vapor density. The vapor phase is compressible whereas the liquid phase is purely incompressible. This again leads to variable density Navier-Stokes equations with strong coupling between the pressure-velocity-density [15]. To compare with the discrete bubble model, in the present work, we do not consider the pressure-velocity-density coupling. Instead the dynamics of vapor production and destruction is simulated in a passive manner similar to the 'one-way' coupling approach used in the discrete bubble model. The effect of pressure-velocity-density coupling (in the scalar-transport model) and the void fraction variations (in the discrete bubble model) on cavitation will be investigated in the future.

3 COMPUTATIONAL APPROACH

An energy-conserving scheme for unstructured, arbitrarily shaped grid elements is used to solve the fluid-phase equations [25–27]. The velocity and pressure are stored at the centroids of the volumes. The cell-centered velocities are advanced

in a predictor step such that the kinetic energy is conserved. The predicted velocities are interpolated to the faces and then projected. Projection yields the pressure potential at the cell-centers, and its gradient is used to correct the cell and face-normal velocities. A novel discretization scheme for the pressure gradient was developed by Mahesh *et al.* [25] to provide robustness *without numerical dissipation* on grids with rapidly varying elements. This algorithm was found to be imperative to perform LES at high Reynolds number in complex flows. A numerical solver based on this approach was developed and shown to give very good results for both simple [28] and complex geometries [27] and is used in the present study.

Scalar Transport: For the scalar-transport model, a scalar field is advected according to equation 10 using a third-order weighted, essentially non-oscillatory (WENO) scheme. The source terms in the scalar transport equation are treated explicitly, whereas the advection terms are treated implicitly. Computation of the scalar transport equation is less expensive and straight-forward to implement.

Discrete Bubble Model: In presence of large variations in the outside pressure, the bubble radius (R_b) and $\frac{dR_b}{dt}$ can change rapidly. Use of a simple explicit scheme with very small time-step can be prohibitively expensive even for a single bubble computation. An adaptive time-stepping strategy is necessary such that the bubble collapse and rapid expansion regions utilize small time-steps, but a much larger time-step can be used for relatively slow variations in bubble radius. An adaptive time step algorithm using the stability criteria of the solution is developed. The stability criterion is based on the eigenvalues of the ODE (equation 5). The equation for bubble radius variations can be cast into two first order ODEs [11]:

$$\frac{dR_b}{dt} = y; \quad \frac{dy}{dt} = -\frac{3y^2}{2R_b} + \frac{P_b - \bar{P}_{out} - 2\sigma/R_b}{\rho_\ell R_b} - \frac{4\mu_\ell y}{\rho_\ell R_b^2}. \quad (13)$$

This can be written in a matrix notation $[X]' = [F]$ where $[X]'$ and $[F]$ are 2×1 matrices. Following the above notation, for example, the forward Euler discretization is given by

$$[X]^{n+1} = [X]^n + h[F]^n = (1 + h[J]^n)[X]^n \quad (14)$$

where h is the step size, n and $n + 1$ denote the current and next time steps, respectively, $[J]^n$ is the Jacobian evaluated at time t_n . The above algebraic system of equations can be diagonalized:

$$[Z]^{n+1} = [\lambda]^n [Z]^n \quad (15)$$

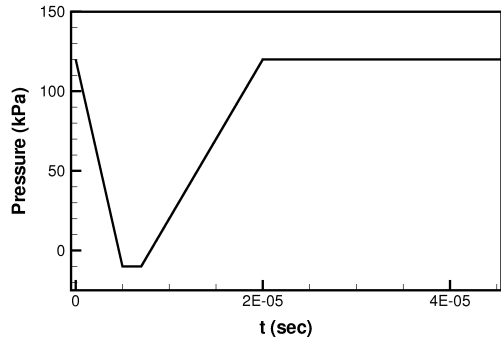
where λ is the matrix of eigenvalues ($\lambda_1 =$ and λ_2) associated with R_b and dR_b/dt , respectively. The solution of equation 15 is of the form: $Z_1^n = e^{\lambda_1} Z_1^0$ and $Z_2^n = e^{\lambda_2} Z_2^0$. The adaptive time-stepping strategy here is therefore, to keep the magnitude of λ_1

and λ_2 close to 1. This λ calculation is used to correct the time step if its deviation from 1 is more than 5%. This strategy is found to be very effective especially in the case of rapid pressure variations. Extensive tests on accuracy and robustness of the numerical algorithm were performed [17]. A sample test case is discussed here.

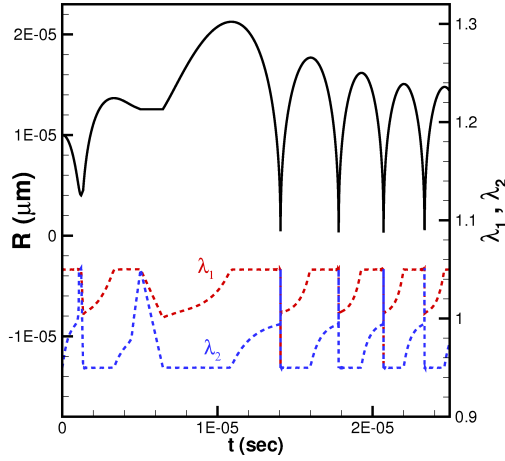
Robustness of the Adaptive Time-Stepping: To test the adaptive time-stepping approach, a numerical test case is considered wherein the external pressure is specified as a function of time and the bubble radius is computed using the Rayleigh-Plesset equation. This test case was first used by Qin *et al.* [11] in their work on simulating cavitating bubbles in a convergent divergent nozzle. Figure 1a shows an imposed pressure variation to a stationary bubble. The fluid properties are those for water ($\rho_\ell = 1000 \text{ kg/m}^3$, $\mu_\ell = 0.798 \times 10^{-3} \text{ kg/ms}$, $\sigma = 0.072 \text{ N/m}$, $p_v = 0.00424 \text{ MPa}$). A bubble of initial radius ($R_{b,0} = 100 \mu\text{m}$, $dR_{b,0}/dt = 0$) is subjected to the outside pressure variation shown in figure 1a. The bubble undergoes growth and collapse as the outside pressure decreases and increases with time. Rapid accelerations and variations in bubble radius are observed.

This test case is challenging for a numerical scheme based on constant time-steps mainly because of a rapid change in outside pressure over a short period of time (outside pressure decreases from 120 kPa to around -10 kPa over $5 \mu\text{s}$). For an explicit Euler scheme, for example, a constant time-step on the order of 10^{-17} s would be required to capture the bubble growth and collapse and maintain a stable solution. Multiple periods of bubble oscillation would be prohibitively expensive for such an approach and adaptive time-stepping is essential. Figure 1b shows the solution obtained from the adaptive time-stepping. Also shown are the temporal variations in the eigenvalues λ_1 and λ_2 of the the coupled system of equations 13. Deviation of these eigenvalues from a value of unity correspond to rapid growth or decay period of the bubble and are good indicators for adaptive time-stepping. The time-step is thus changed if the eigenvalues depart from the unity value by 5% or more. With this approach stable solutions are obtained for much higher time-steps and multiple periods of bubble oscillation can be easily computed. Figure 1c shows that only around 2000 iterations are required to compute five periods of bubble oscillation for this test case with very large pressure variations. A time-step refinement study provided little variations in the predictions.

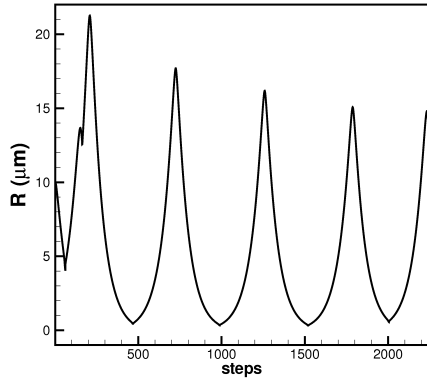
Sub-cycling of Bubble Transport Equations: The time-step for discrete bubble model (δt_{bub}) obtained based on the above adaptive strategy is compared with the flow-solver time-step (δt_{solver}). A sub-cycling procedure is used, wherein the bubble time-step is maintained *five-times* smaller than the flow-solver time-step, and the bubble dynamics equations are solved repeatedly until we reach one δt_{solver} . Accordingly, the actual time-step



(a) Imposed outside pressure



(b) $R(t)$, $\lambda_1(t)$, $\lambda_2(t)$



(c) Number of iterations

Figure 1: A numerical test case to study the effectiveness of the adaptive time-stepping algorithm: (a) time variation of the imposed outside pressure; (b) time variations of bubble radius (R_b) and eigenvalues (λ_1 , λ_2), (c) bubble size variations with respect to the number of iterations.

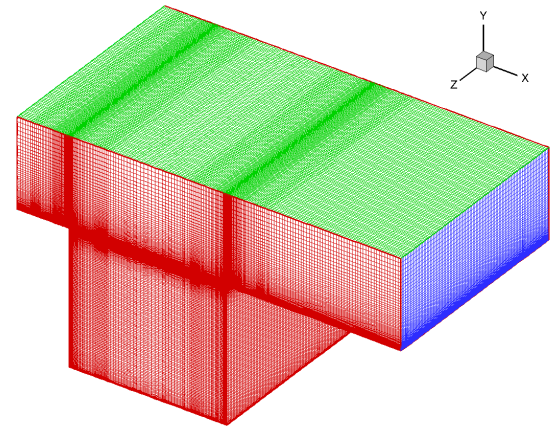
for bubble dynamics is then obtained as:

$$\delta t = \min\left(\delta t_{bub}, \frac{\delta t_{solver}}{5.0}\right) \quad (16)$$

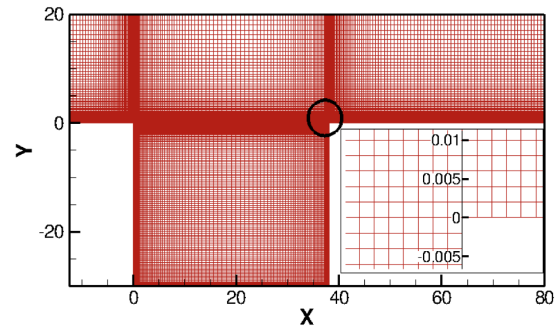
For the bubble position and the velocity field the same time-steps are used. The bubble position and velocity fields are updated using a third-order Runge-Kutta scheme; the bubbles are duly transferred across processors as their positions are updated.

4 NUMERICAL SETUP

The numerical setup consists of a straight ducted channel with a nearly square cavity in the central region as shown in figure 2. To keep the computational size small, we only simulate up to the half duct height. Emphasis is placed on the shear layer and the leading and trailing edges of the cavity, with refined grids in these regions. The computational domain includes the cavity and the duct flow which starts at -12.4 mm before the cavity leading edge and ends at 32 mm after the trailing edge.



(a) 3D View



(b) Symmetry Plane

Figure 2: Computational domain and grid: (a) three-dimensional domain with Cartesian grid, (b) refined grids (dimensions shown are in mm) are used in the shear layer and near the cavity leading and trailing edges. A zoomed-in view of the grid near the trailing edge is shown in wall co-ordinates.

Table 1 gives the details of the computational domain size and the grid resolutions. The grid elements are mainly Cartesian hexahedra with refined regions in the leading edge and near wall regions. The wall-layers in the leading and trailing edges are resolved.

Table 1: Computational domain and grid size (+ denotes wall units).

Cavity size	$38.1 \times 30 \times 50.8$	mm^3
Channel size	$92.4 \times 20 \times 50.8$	mm^3
$\Delta x_{min} = \Delta y_{min}$	$1.9 \mu\text{m}$	
$\Delta x_{min}^+ = \Delta y_{min}^+$	1.1	
Δz & Δz^+	$500 \mu\text{m}, 208$	
Cavity length L	38.1 mm	
Total grid points	5 million	
Reynolds number	$Re_L = 170,000$	
Average inflow velocity	$U_\infty = 5 \text{ m/s}$	
Simulation time step	$\delta t_{solver} = 10^{-4} \text{ ms}$	
Vapor pressure	$P_v = 2.337 \text{ kPa}$	

4.1 Boundary Conditions

In the present simulation, the wall layers are resolved, and no-slip conditions are applied at all walls. A convective outflow boundary condition is applied at the outlet. In the experimental setup, the upstream region of the duct consists of a convergent section near the bottom wall and the flow is tripped using thirteen notches to create turbulence [1]. The divergent section is not simulated in the present study. Instead, it is assumed that the flow is fully developed and the experimentally measured mean velocity field in the symmetry plane is used to specify the inlet conditions. To create proper turbulence structures, a separate periodic flow in a duct is simulated at the desired mass-flow rate and Reynolds number using a body-force technique [29]. The Reynolds number based on the friction velocity for the inflow duct is very high ($Re_\tau = 7500$). We perform a highly resolved LES of a periodic duct flow on $180 \times 256 \times 144$ grid points with the resolution of $\Delta x^+ = 64$, $\Delta z^+ = 42$, and $\Delta y_{min}^+ = 0.835$, $\Delta y_{max}^+ = 85$ (where the superscript ‘+’ denotes wall variables). Figure 3 shows the comparison of the vertical variations of mean and *rms* axial velocity field in the symmetry plane with the experimentally measured inlet flow. A reasonable agreement is obtained for the *rms* fluctuations; however, the mean flow shows much higher shear in the experiment than those obtained from the simulations. In the experiments, there was also a significant amount of vertical ve-

locity in the downward direction, possibly obtained because of the convergent section in the upstream part of the duct. To match the mean flow with the experimental data, we use the mean flow field from the experiments and the instantaneous velocity fluctuations from the periodic duct flow as inlet boundary condition:

$$u_i^{\text{inflow}} = (\overline{u_i^{\text{periodic duct}}} - \overline{u_i^{\text{periodic duct}}}) + \overline{u_i^{\text{experiment}}}, \quad (17)$$

where $\overline{(\quad)}$ in the above expression denotes time-averaged quantity. The superscript ‘periodic duct’ stands for flow field from the highly resolved periodic duct flow. This inflow data over several flow through times is generated *a priori* and read at each time step to specify the velocity components at the inlet. This technique ensures that the fluctuating velocity field at the inlet section is divergence-free. Later, we show the effectiveness of the inflow velocity fluctuations in predicting the flow statistics downstream. In order to obtain good predictions from the LES computation, an accurate estimation of the inflow conditions is necessary. With this approach, the inflow conditions are better represented in the computations. The predictive capability of LES can now be tested by comparing the flow features and turbulence statistics with the experimental data.

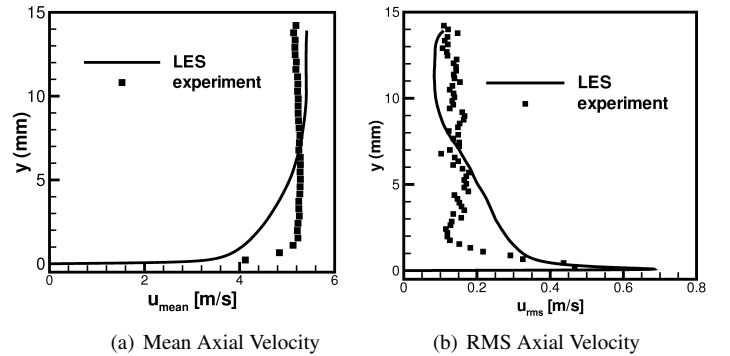


Figure 3: Comparison of vertical variations of mean and *rms* axial velocity fields in the inflow section (obtained from a stand-alone LES computation of a periodic duct flow) with the experimental data [1]. For inlet conditions, we use the mean velocity profiles from the experiments and fluctuating velocity field from the periodic duct flow.

5 NUMERICAL RESULTS

We first compare the flow statistics obtained from the simulation, including mean and *rms* values of the flow field, to those reported in LK2008. Inception studies based on discrete bubble and scalar transport models are performed next. Detailed comparisons of flow statistics between LES and experimental data are presented.

5.1 Leading Edge

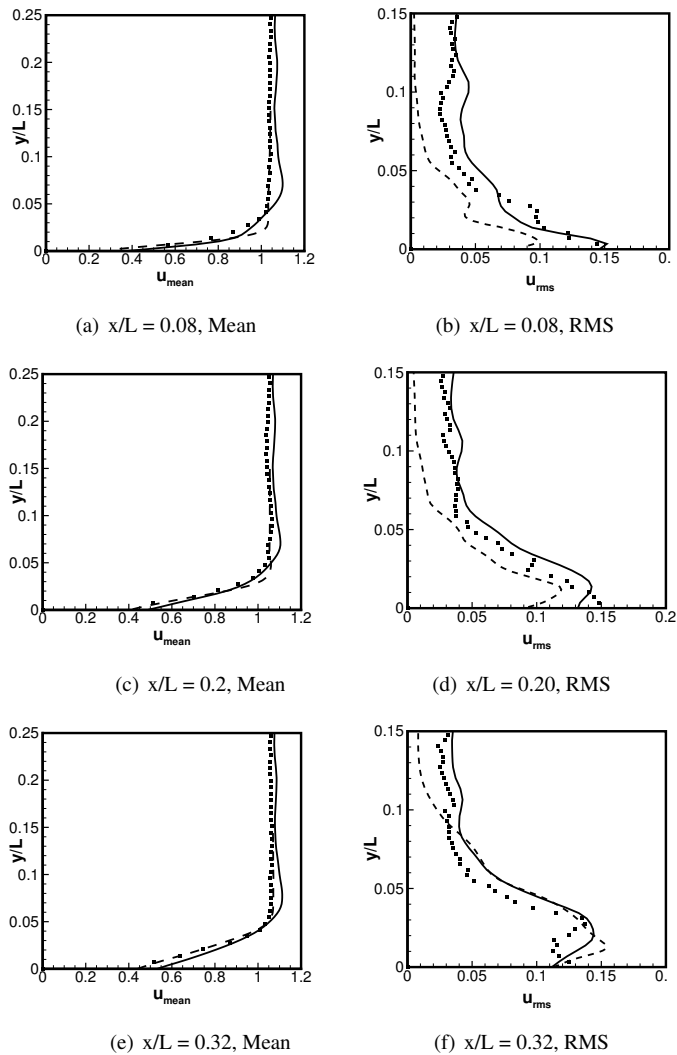


Figure 4: Comparison of vertical variations of stream-wise fluctuations near the leading edge with (solid lines) and without (dashed lines) inflow fluctuations with the experiment data of LK2008 (symbols).

Figure 4 shows comparison of the vertical variations in the mean and *rms* axial velocity field near the leading edge with the data of LK2008. LES predictions with and without inlet velocity fluctuations are shown at three different locations. The mean flowfield is reasonably well predicted by both computations. It is slightly better predicted when only the experimental mean flow was used (without any fluctuations). However, the *rms* velocity fields are much better represented by LES with inlet flow fluctua-

tions. Specifically, the *rms* fluctuations disappear away from the wall in the absence of imposed inflow fluctuations. The experimental data as well as LES with inflow fluctuations show substantial turbulence further away from the wall. The distribution of the *rms* velocity fields are also better predicted by the LES with inflow fluctuations. It was observed that with no fluctuations at the inlet, flow structures above the shear layer generally predicted very low levels of turbulence. Accurate characterization of the inlet flow fluctuations are thus found to be important. An LES simulation inclusive of the upstream divergent section at the bottom wall of the duct may provide even better inflow conditions.

5.2 Trailing Edge

Contour plots of the normalized mean axial velocity (\bar{u}/U_∞) and vertical velocity (\bar{v}/U_∞) are presented in figure 5. Also shown are the distribution of axial velocity in the vertical direction near the trailing edge compared to the data of LK2008. The distribution of the mean velocity field is very similar to that shown by LK2008. It is observed from the mean streamtraces that the shear layer impinges the trailing edge slightly below the corner. The LES results predict the behavior of the mean axial velocity reasonably well above the trailing edge. Upstream of the trailing edge (inside the cavity), the experimental data indicates slightly lower axial velocity than those predicted by the LES ($x/L = 0.8, 0.9$). A more refined grid in the axial direction over the entire shear layer may be necessary to capture the high shear in this region.

The distribution of the mean pressure near the trailing edge is shown in figure 6. Also shown are locations of eight probes (p1–p8) at which the pressure signal is further analyzed. The following two features also observed in the experiments are accurately predicted: (i) a high-pressure region just upstream of the trailing edge (corner in the present 2D plane) which extends into the cavity, and (ii) a low pressure region above the trailing edge. The high pressure region just upstream of the trailing edge occurs basically due to the impingement of the shear layer onto to the trailing edge, creating a stagnation point slightly below the edge. The flow then has to turn and go around, creating a low pressure region above the trailing edge. The shape of contours of the mean C_p are similar to those observed in the experiments.

The probability distribution functions (PDFs) of the fluctuations in pressure coefficient (C'_p) at the eight probes are shown in figure 7a-h. The corresponding mean and *rms* values of C_p are also quoted. Probes p1 and p2 are slightly upstream of the trailing edge, probes p3 and p4 are in the shear layer, and probes p5–p8 are downstream of the trailing edge. Based on the mean values of C_p and PDFs of C'_p , cavitation is likely to occur inside the shear layer for a cavitation index of $\sigma_i \leq \sim 0.43$ (for example, for probe p3, $\bar{C}_p = -0.13$ with a PDF tail of around -0.3). LK2008 also observed cavitation inside the shear layer for similar inception index. The mean statistics were collected over 4

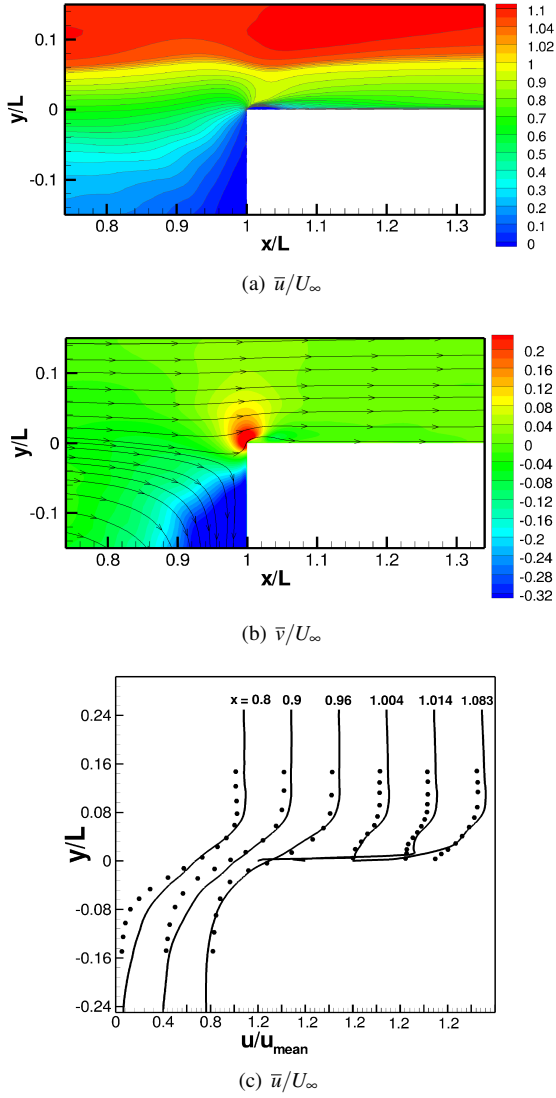


Figure 5: Contours of time-averaged velocity fields near the trailing edge: (a) mean axial velocity field, (b) mean vertical velocity field together with streamlines, (c) vertical variation of mean axial velocity with the experimental data of LK2008.

flow through times (that is over around 33 ms where one flow through time is taken to be approximately $L/U_\infty \sim 7.7$ ms. This is rendered sufficient time for the shear-layer statistics.

The probes (p5–p8) above the trailing edge (downstream of the corner) show low values of \bar{C}_p together with a broader spectrum of C_p' . Inception first occurs inside these regions as also noted by LK2008. It is observed that in the present simulations, the absolute values of mean pressure coefficient ($|\bar{C}_p|$) at some points above the trailing edge (i.e. probes p5–p8) were generally higher and the *rms* values ($C_{p,rms}$) were lower compared to the experimental data. For example, at probe p6, $\bar{C}_p = -0.63$ and $C_{p,rms} = 0.3$ providing an inception index of $\sigma_i = 0.93$. LK2008

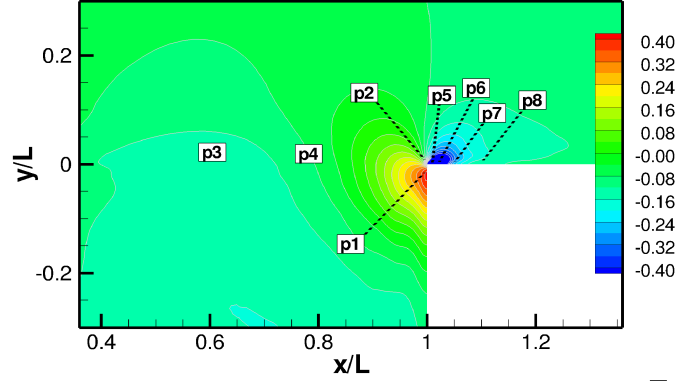


Figure 6: Time-averaged contours of pressure coefficient (\bar{C}_p) near the trailing edge.

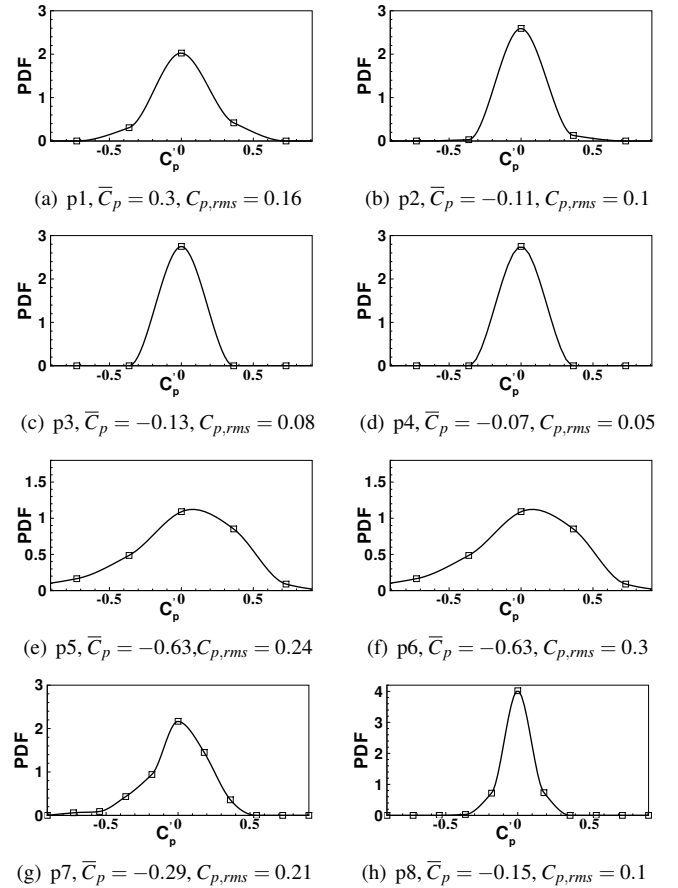


Figure 7: Probability distribution functions for C_p' at the eight probe locations (p1–p8) shown in Figure 6.

also reported inception index of $\sigma_i = 0.9$; however, generally showed lower mean C_p and higher C_p' above the trailing edge. In LES, the PDFs of C_p' showed larger negative tails. If instantaneous values of C_p are used as criterion for inception, these

distributions indicate that inception above the trailing may occur at even higher σ_i values. In experiments, the pressure signal was deduced based on the material acceleration $D\mathbf{u}/Dt$ by neglecting the viscous effects [30]. In LES, near the trailing edge, the viscous effects may be small; however, the subgrid-scale stresses can be large influencing the filtered pressure field as:

$$-\frac{1}{\rho_\ell} \nabla \bar{P} = \frac{D\bar{\mathbf{u}}}{Dt} - \frac{\partial \tau_{ij}^r}{\partial x_j}. \quad (18)$$

It is conjectured that local variations in subgrid-scale stresses and subgrid viscosity obtained from the dynamic model may affect the filtered pressure field resulting in lower pressure values in a small region above the trailing edge. However, away from the trailing edge, the pressure coefficients were well predicted compared to the experiments. The variations in C_p values above the trailing edge were related to the impacting of shear layer vortices on the trailing edge and is discussed below.

5.3 Instantaneous Flow Field

Figure 8 shows the instantaneous plots of $C_p = (\bar{P} - P_\infty)/(0.5\rho U_\infty^2)$ in the symmetry plane ($z = 0$) together with instantaneous streamlines obtained by removing $0.5U_\infty$ from the axial velocity field. Low pressure regions within the shear layer and corresponding vortical structures are clearly visible. The two snapshots (8a,b) correspond to higher and lower pressures just above the trailing edge corner ($x/L = 1.01$, $y/L = 0.0035$, $z/L = 0$). The instantaneous C_p signal at this location is also shown in figure 8d. The vortical structures in the shear layer generated from the leading edge separation travel downstream and interact with the trailing edge causing significant changes in the C_p values above the trailing edge. Liu and Katz [1] showed similar vortex structures and argued that there is a strong correlation between the traveling vortices and the trailing edge, causing flow-induced C_p fluctuations. We observed similar interactions between the traveling vortices and the trailing edge. Based on the signal shown in figure 8d, the C_p value varies over a wide range of -0.01 to -2 . The C_p values also showed variations in the spanwise directions suggesting that the impact location of the vortex cores on the trailing edge (and the stagnation point) move in and out of the plane (in spanwise directions). Based on the mean and *rms* values of the pressure coefficient at neighboring points ($\bar{C}_p \sim -0.639$, $C_{p,rms} \sim 0.29$), the inception index is approximately $\sigma_i \sim 0.93$.

5.4 Cavitation Inception

We consider two different approaches to investigate the nature of cavitation near the trailing edge and inside the shear layers: (i) a discrete bubble model and (ii) a scalar transport model. In the discrete bubble model, it is assumed that water contains abundant nuclei of dissolved gas which can undergo rapid size

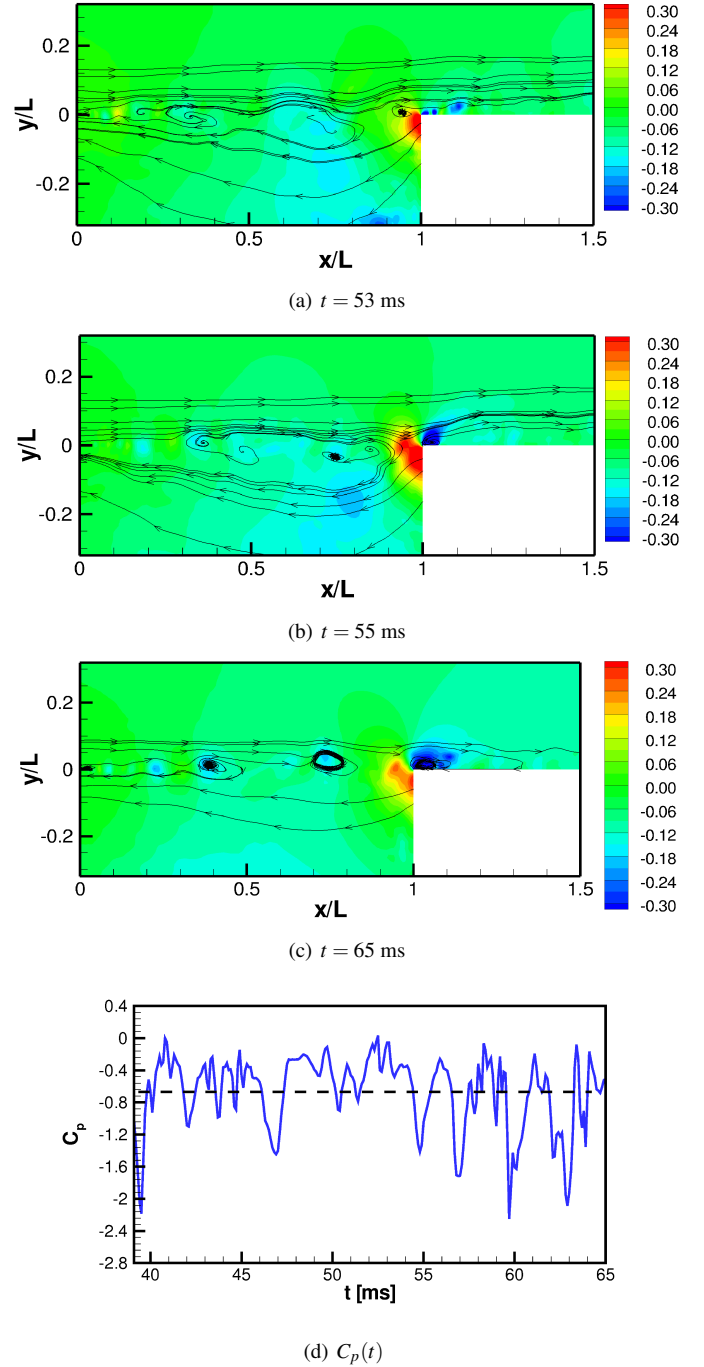


Figure 8: Instantaneous pressure contours and stream traces (based on removing $0.5U_\infty$ from the streamwise velocity):(a) $t = 53$ ms (high pressure above the trailing edge), (b) $t = 55$ ms (low pressure above the trailing edge), (c) $t = 65$ ms, (d) $C_p(t)$ at a probe above the trailing edge ($x/L = 1.01$, $y/L = 0.0035$, $z/L = 0$).

variations indicating occurrence of cavitation. In the scalar transport model, actual phase change is simulated by modeling rates of evaporation and condensation based on the local pressure field compared to the vapor pressure. Results obtained from both models are presented below.

Scalar Transport Model: For the scalar-transport model, a transport equation for liquid volume fraction (equation 10) is solved as described earlier. The source and sink terms in the transport equation are proportional to the difference between the local pressure and the vapor pressure as well as the amount of liquid present in a given control volume. Typically, if the local pressure drops below the vapor pressure, the liquid evaporates creating vapor. In the present work, the local pressure field was defined relative to the pressure field above the leading edge of the cavity (P_∞). Similarly to the experiments, the absolute value of P_∞ was reduced starting with one atmosphere. The vapor pressure was assumed to be $P_v = 2.337$ kPa. Early sites of cavitation occurred above the trailing edge where the pressure minima occurs. Small amounts of vapor were created in this region with vapor fractions on the order of 0.01 for a cavitation index of $\sigma_i = 0.9$. Further reduction in P_∞ resulted in increased cavitation above the trailing edge.

Figure 9 shows the temporal evolution of the vapor fractions ($\phi = 1 - \Theta_\ell$) above the cavity trailing edge when the upstream pressure (P_∞) was set based on the inception index of $\sigma_i = 0.4$. In the experiments, vigorous cavitation was observed at this level. A top view is shown with a slice at distance $y = 0.01$ mm in the wall-normal direction. Periodic occurrence and disappearance of vapor fraction structures above the trailing edge are clearly visible (dark regions show large vapor fraction). A time trace of instantaneous ϕ and C_p are plotted in figure 10. The frequency of the growth and decay of vapor fraction is observed to be around 300 Hz for the present case with $U_\infty = 5$ m/s. As can be seen from the contour plots and the time traces, periodic occurrence and disappearance of cavitation is predicted similar to that observed in experiments. This indicates that this periodic cavitation phenomenon is associated with the pressure variations above the trailing edge. The pressure variations are mainly caused by the shear-layer eddies impinging on the the cavity trailing edge (see figures 8). In the present work, we do not have pressure-velocity-density coupling, which may become important when heavy cavitation occurs (for the case of $\sigma_i \leq 0.4$). However, the features associated with periodic growth and decay of the vapor fraction above the trailing edge are captured.

Discrete Bubble Model: We also performed cavitation inception studies using the discrete bubble model (DBM) with adaptive time-stepping as described earlier. The gas content in the liquid was assumed to be small (initial gas void fraction was assumed to be 10^{-5}). It is important for the bubble nuclei to pass through the small pressure regions above the cavity ('window of oppor-

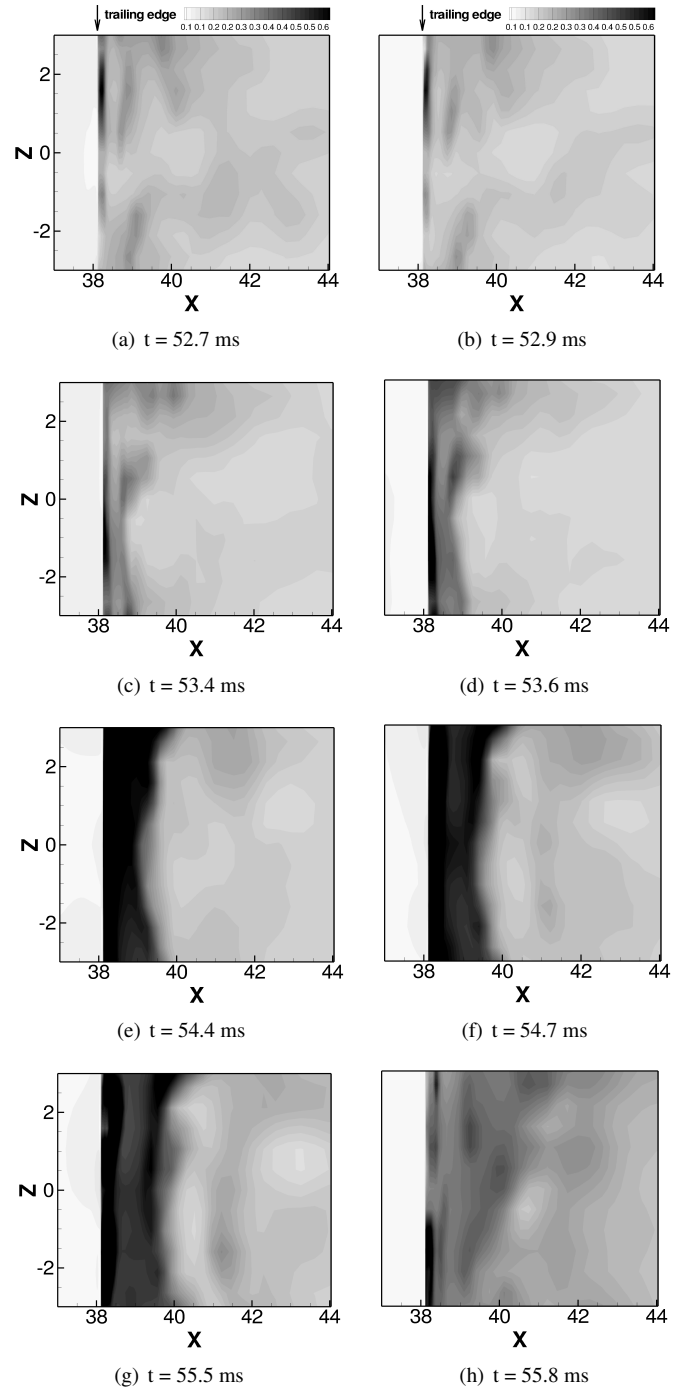


Figure 9: Evolution of liquid vapor fraction ($\phi = 1 - \Theta_\ell$) above the trailing edge as predicted by the scalar transport model. Periodic growth and decay of the local vapor fraction is correlated with the variations in C_p just above the trailing edge.

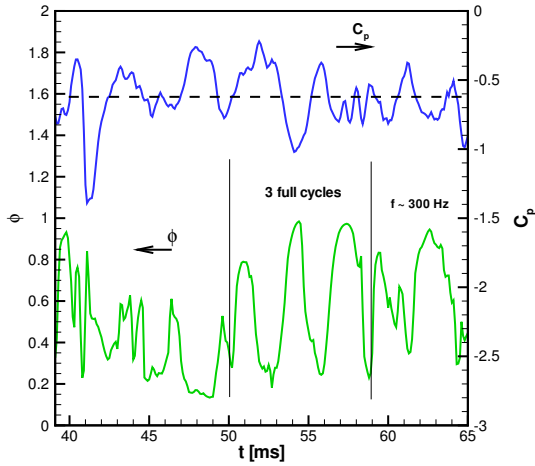


Figure 10: Time evolution of vapor fraction and C_p just above the trailing edge at $\vec{x} = (38.1, 0.01, 0.0)$ for $\sigma_i = 0.4$.

small region in stream-wise direction and in a band of 10 mm in the mid section of flow span. In order to keep the number of bubbles constant in the domain, bubbles were continuously injected near the leading edge and removed farther away from the trailing edge. To analyze the sensitivity of the initial bubble size to cavitation inception, detailed PDF analysis (following the works of Cerutti *et al.* [8] and Kim *et al.* [9]) was performed by collecting data over 1.8 flow through time based on the cavity length and the free-stream velocity.

Table 2: Case studies to analyze cavitation inception using the Discrete Bubble Model.

Case	Figure Symbol	d_{initial} (μm)	σ_i
C1	square	10	0.4
C2	triangle	50	0.4
C3	circle	100	0.4
C4	diamond	50	0.9
C5	circle (filled)	50	1.4

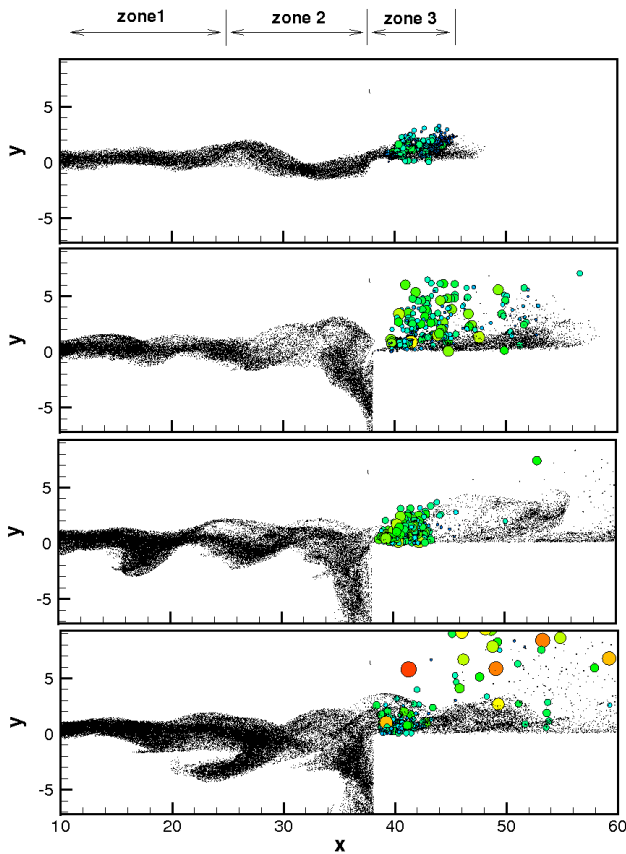
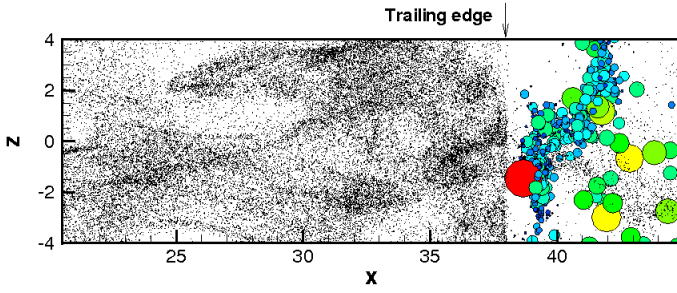


Figure 11: Temporal evolution of bubble distribution (initial size $50 \mu\text{m}$) on the shear layer (side view) for $\sigma_i = 0.4$.

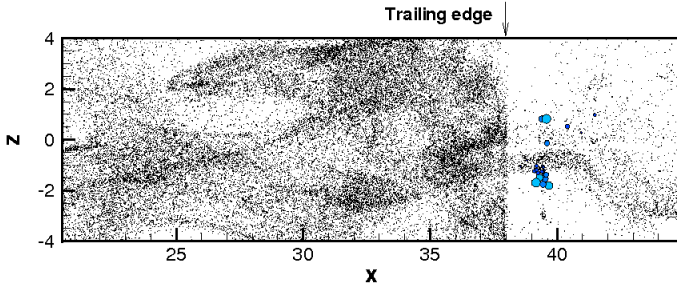
Figure 11 shows the temporal evolution of bubble locations inside the shear layer and above the trailing edge. The size of the scatter symbols is scaled with respect to the size of the bubble. Accordingly, large size bubbles are obtained near the trailing edge. The initial pressure inside the bubble was set based on an equilibrium radius corresponding to the radius of the nuclei and its location in the domain. Using the Rayleigh-Plesset equations (13), at equilibrium conditions, the pressure inside the bubble can be obtained as: $P_b = \bar{P}_{out} + 2\sigma/R_b$ (σ is the surface tension coefficient). The bubbles are then advected using the adaptive time-stepping described earlier with ‘one-way’ coupling (bubbles do not affect the flow). On an average, approximately 50,000 bubble trajectories are tracked at each instant. In order to gain better understanding of how different parameters such as the initial bubble size and cavitation index σ_i affect the inception and the behavior of bubbles, three different initial bubble sizes (10, 50, and $100 \mu\text{m}$) were considered with a constant cavitation index ($\sigma_i = 0.4$). In addition, three different cavitation indices (0.4, 0.9, and 1.4) were examined on a certain initial bubble diameter ($d_{\text{init}} = 50 \mu\text{m}$). Table 2 shows different diameters and cavitation indices used in the present study.

tunity’ to get drawn into low pressure regions and cavitate) [6]. Accordingly, air nuclei were distributed evenly in a small band around the shear layer. The bubbles were initially injected over a

Figure 12 shows instantaneous snapshots (a top view) of bubbles just in the the shear layer and above the trailing edge (only a few bubbles are shown for clarity). The bubble size is scaled according to their diameter; thus bubbles with large radius



(a) $\sigma_i = 0.4$



(b) $\sigma_i = 0.9$

Figure 12: Top view of the instantaneous snapshot of bubbles above in the shear layer and near the trailing edge: (a) absolute value of outside pressure based on $\sigma_i = 0.4$, (b) outside pressure based on $\sigma_i = 0.9$.

appear more prominently. The two sets of snapshots correspond to different values of P_∞ (set based on the cavitation index (σ_i) of 0.4 and 0.9). For $\sigma_i = 0.4$ large size bubbles are readily observed near the trailing edge. As shown later, rapid variation in bubble size occurs near the trailing edge. As shown later, for this inception index, bubbles inside the shear layer also showed growth in their size. For higher pressure at the upstream ($\sigma_i = 0.9$; figure 12b), bubbles cavitate near the trailing edge; however, little change in size of the bubbles was observed inside the shear layers.

Data Sampling: To analyze the effect of various model parameters, we collected probability distribution functions (PDFs) of number of bubbles based on their growth ratio d/d_{initial} , the pressure coefficient C_p , and the vorticity ω at bubble position. Three different initial bubble sizes were considered (cases C1, C2, C3), and for initial bubbles of $50 \mu\text{m}$ the cavitation index was varied ($\sigma_i = 0.4, 0.9$, and 1.4) in cases C2, C4, and C5. In addition, we looked at different regions in the flow (labeled as zones as shown in figure 11). The criteria for the location are $-5\text{mm} < y < 5\text{mm}$ in three different zones in streamwise direction: $-2\text{mm} < x < 25\text{mm}$, $25\text{mm} < x < 38\text{mm}$, and $38\text{mm} < x < 45\text{mm}$, which are being referred to as zone 1, 2, and 3. We have also performed conditional sampling on the parameters based on bubble growth ratio (d/d_{initial}), and location.

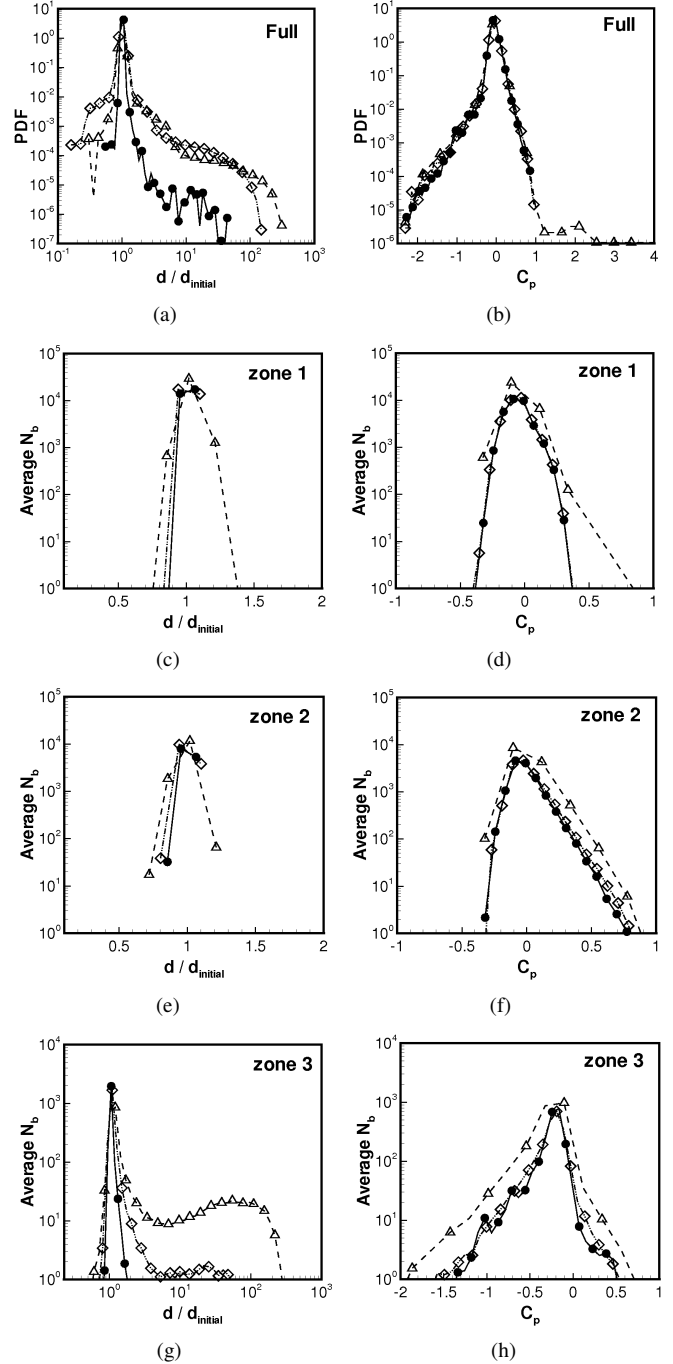


Figure 13: Effect of cavitation index σ_i on the PDFs and average number of bubbles (N_b) sampled based on the growth ratio (d/d_{initial}) and pressure coefficient C_p for case C2 (triangle symbols), C4 (diamond symbols), and C5 (filled circles): (a,b) PDF of all bubbles over the region of interest; (c,d) bubbles in zone 1; (e,f) bubbles in zone 2, and (g,h) bubbles in zone 3.

For the growth ratio condition we defined three different zones of $d/d_{\text{initial}} < 0.8$, $0.8 < d/d_{\text{initial}} < 1.25$, and $1.25 < d/d_{\text{initial}}$, referred to as small, medium, and large. For the PDF calculations, data spans (minimum to maximum of each parameter) have been divided into 41 different bins which are distributed logarithmically for diameter and linearly for pressure and vorticity. Samples collected over several instantaneous snapshots were averaged and these results are discussed below.

Effect of Cavitation Index: Figure 13 shows the effect of cavitation index on the PDFs and number of bubbles sampled based on the bubble growth ratio (d/d_{initial}) and the pressure at the bubble location in various regions of the shear layer and the trailing edge. These plots are obtained with fixed initial bubble size of $50 \mu\text{m}$. In figure 13(a) we observe that a majority of the bubbles retain their original size and are mostly insensitive to pressure variations ($d/d_{\text{initial}} \sim 1$). With lower cavitation index ($\sigma_i = 0.4$), the maximum bubble growth ratio is higher, and a small number of very large bubbles are observed near the trailing edge (giving rise to cavities on the order of 0.1-0.5 cm). This is due to the effect of lower pressure on the bubbles compared to the cases with $\sigma_i = 0.9$ and 1.4. The other important difference is on the left tail of PDF (collapse region) where the PDF of growth ratio is almost an order of magnitude larger for $\sigma_i = 0.9$ compared to $\sigma_i = 0.4$. This again indicates violent cavitation for lower cavitation index. Next we consider the behavior of bubbles in different regions of the flow: near the leading edge (zone 1), in the mid-section (zone 2) and over the trailing edge (zone 3). Figures 13c-h show average number of bubbles sampled based on the growth ratio and C_p values. In zones 1 and 2 (i.e. inside the shear layer), there is small change in the average number of bubbles versus a certain growth ratio for different cavitation indices; however, for $\sigma_i = 0.4$ more variation in bubble sizes were observed in both zones (figures 13(c),13(e)). Near the trailing edge, large differences in the number of bubbles with the same growth ratio are observed (figure 13(g)). For the lowest σ_i (C2), number of large bubbles observed near the trailing edge is at least an order of magnitude more than other cases (C4 and C5). The highest cavitation index nearly shows no cavitation above trailing edge.

Figure 13(b) shows the PDF of C_p at bubble locations for cases C2, C4, and C5 over the entire region of interest. Changing σ_i doesn't change the PDF curves sampled based on C_p appreciably; implying that the location of bubbles is not significantly affected by varying σ_i . This can also be observed in the snapshots of bubbles in figure 12. Figures 13(d), 13(f), and 13(h) show the average number of bubbles sampled based on C_p in zones 1 (near leading edge), 2 (mid section), and 3 (near trailing edge), respectively. Noticeable number of bubbles are observed in the range of $-1 \leq C_p \leq 1$. This is consistent with the experiments, wherein Liu and Katz [1] predicted cavitation inception occurs at $\sigma_i = 0.9$. These plots also indicate presence of large number of bubbles in the low pressure region for $\sigma_i = 0.4$. Based on the

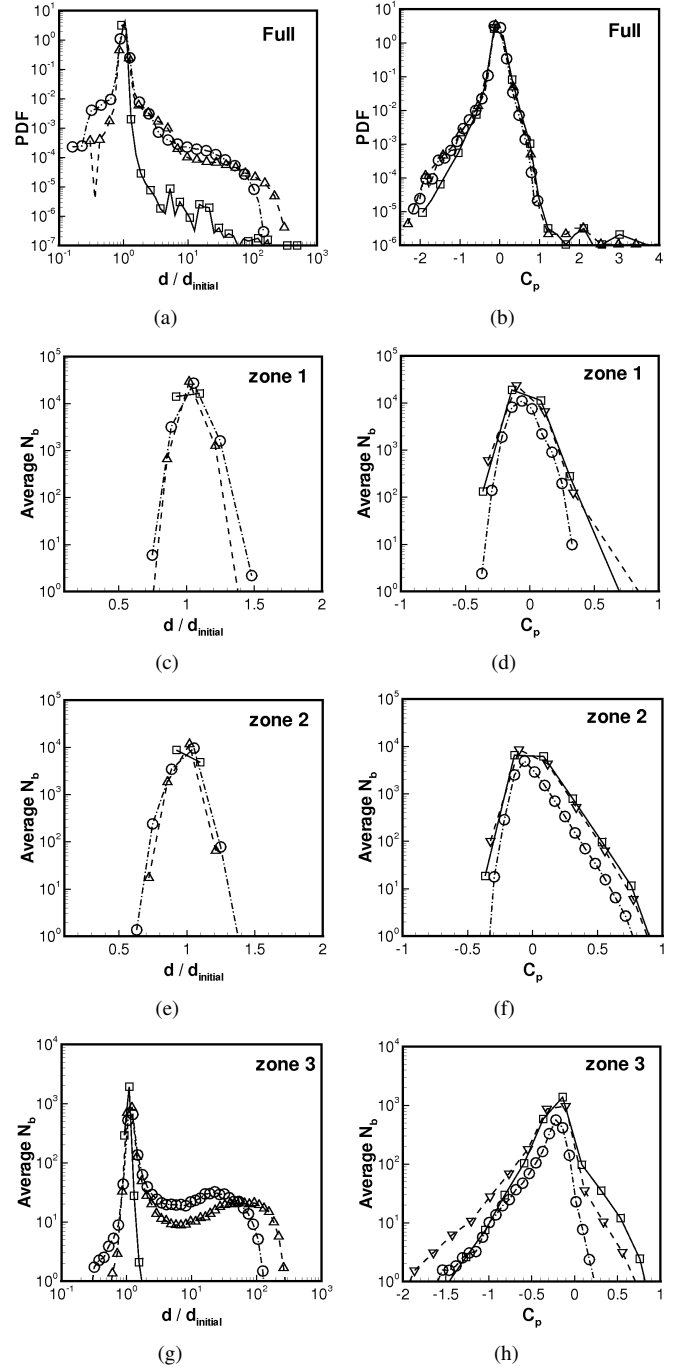


Figure 14: Effect of initial bubble size on the PDFs and average number of bubbles sampled based on growth ratio (d/d_{initial}) and pressure coefficient C_p at bubble location for cases C1 ($10 \mu\text{m}$ square symbols), C2 ($50 \mu\text{m}$ triangle symbols), and C3 ($100 \mu\text{m}$ circle symbols): (a,b) PDF for all bubbles over the region of interest; (c,d) bubbles in zone 1; (e,f) bubbles in zone 2, and (g,h) bubbles in zone 3.

growth ratios, these are typically larger size bubbles which get attracted toward the low pressure region.

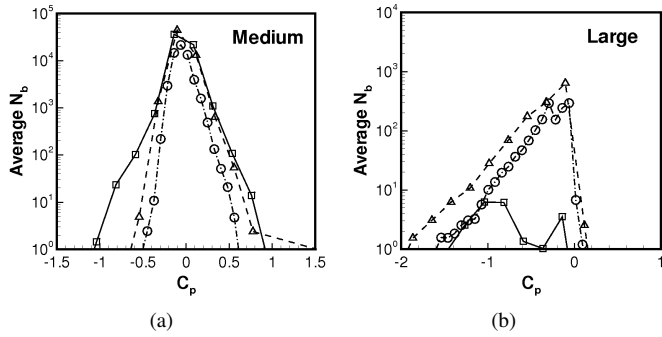


Figure 15: Average number of conditionally sampled bubbles based on pressure coefficient at bubble location for case C1 (square), C2 (triangle), and C3 (circle): (a) medium size group ($0.8 < d/d_{\text{initial}} < 1.25$), (b) large size group ($1.25 < d/d_{\text{initial}}$).

Effect of Initial Bubble Size: The effect of initial bubble size is shown in figures 14. In these figures we also look at PDFs of growth ratio and C_p for cases C1, C2, and C3 over the entire region (figure 14a,b). The average number of bubbles sampled according to their growth ratio and C_p are also shown in three different zones (figure 14c-h)

Figure 14(a) shows that the smaller bubbles (10 micron) are less sensitive to growth. A majority of them grow to about 3-4 times their original size, whereas a very few become 100 times larger. This may be attributed to the fact that smaller bubbles tend to travel with the flow (low Stokes number), and may not get entrained into lower pressure region quickly. Larger bubbles (50 and 100 microns) can grow to very large size (10-100 times the initial size). Based on the growth ratio, 50 and 100 micron bubbles seem to be entrained in the low pressure regions in the shear layer (zones 1 and 2) and show some growth (less than twice the initial size) in these regions for $\sigma_i = 0.4$. Near the trailing edge, however, rapid growth in size is observed for these bubbles; some growing up to 50 times their original size. Correspondingly, they create cavities on the order of 0.5 cm also observed in the experiments.

Conditional Sampling and Bubble Distributions: To further characterize the sensitivity of the bubbles to imposed pressure variations, the bubbles were sampled into three groups based on their growth ratio: small ($d/d_{\text{initial}} < 0.8$), medium ($0.8 < d/d_{\text{initial}} < 1.25$), and large ($1.25 < d/d_{\text{initial}}$) bubbles. Bubbles from each group were then conditionally sampled to obtain PDFs and average number of bubbles based on C_p (figure 15) and vorticity ω distributions (not shown). Figures 15a,b show that bubbles with initial size 10 micron tend to grow into

medium group (i.e. $0.8 < d/d_{\text{initial}} < 1.25$), whereas larger initial size bubbles (50 and 100 micron) exhibit large growth ($1.25 < d/d_{\text{initial}}$). This indicates that bubbles with initial size in the range of 50-100 microns are capable predicting visible cavitation. Similar conclusions were drawn for plots based on vorticity distribution (not shown for space). This indicates that small initial size bubbles although sensitive to pressure fluctuations, do not tend to cluster in regions of high vorticity or low pressure. To predict cavitation inception, initial bubble sizes on the order of 50-100 micron are best suited for this flow as they tend to cluster in low pressure regions and thus can grow to large sizes.

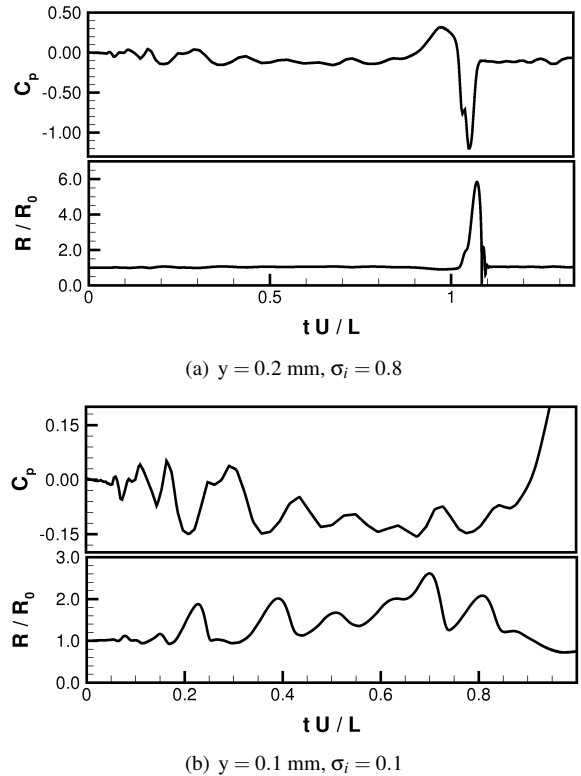


Figure 16: Temporal evolution of bubble radius (normalized by initial radius) and outside pressure coefficient (C_p) seen by the bubbles for two sample trajectories of bubbles released near the leading edge. The upstream pressure level is set based on $\sigma_i = 0.8$ for the top panel and $\sigma_i = 0.1$ for the bottom panel: (a) bubble released at $y = 0.2$ mm, (b) released at $y = 0.1$ mm from the leading edge surface.

Bubble Trajectories: We monitored trajectories of some bubbles that were released near the leading edge. Figure 16 shows the variations in the outside pressure signal (C_p) and the corresponding changes in the bubble radius (R_b) experienced by the bubble as it moves from its injection location. Two sample

bubble trajectories are shown for bubbles released close to the leading edge in the wall-normal direction. The first trajectory (figure 16a) is for outside pressure set based on the cavitation index of 0.8. The bubbles show rapid variations in their size as they encounter the trailing edge low pressure region. The second trajectory (figure 16b) corresponds to bubble dynamics with a much lower upstream pressure ($\sigma_i = 0.1$). This shows cavitation occurring in the shear layer.

6 CONCLUSIONS

We performed LES of turbulent flow over an open cavity corresponding to the experimental setup of Liu and Katz [1] at the flow Reynolds number of 170,000. The filtered, incompressible Navier-Stokes equations were solved using a co-located grid finite-volume solver [27] with the dynamic Smagorinsky model on a five million grid with mainly Cartesian hexahedral elements. The mean flowfield at the inlet section is specified from the experimental data in the symmetry plane, whereas, turbulent fluctuations were imposed at the inflow based on resolved computation of a periodic duct flow keeping the mass-flow rate and the Reynolds number the same. The flow statistics, including mean and rms velocity fields showed reasonable agreement with the experimental data near the leading and the trailing edges. The mean pressure distribution shows two distinct features near the trailing edge: (i) a high-pressure region just upstream of the trailing edge which extends slightly into the cavity, and (ii) a low pressure region above the trailing edge. The high pressure region just upstream of the trailing edge occurs mainly due to the impingement of the shear layer onto the trailing edge, creating a stagnation point inside the cavity. The flow then has to turn and go around the trailing edge creating a low pressure region above the trailing edge. The shape of contours of the mean C_p were very similar to those observed in the experiments and predicted that cavitation inception occurs just above the trailing edge in the low pressure region. Variations in local C_p values above the trailing edge were also investigated and showed correlations with the impingement of the shear layer vortices onto the trailing edge.

Cavitation inception was investigated using two approaches: (i) a discrete bubble model for gaseous cavitation wherein the bubble dynamics is computed by solving the Rayleigh-Plesset and the bubble motion equations using an adaptive time-stepping procedure, and (ii) a scalar transport based model for the liquid volume fraction with source and sink terms for phase change corresponding to vaporous cavitation. In both models, the effect of bubbles or vapor on the flowfield was neglected. Simulations with different values of the outside pressure were performed by changing the cavitation index (σ_i). Both models predicted that inception occurs above the trailing edge. For $\sigma_i < 0.4$, heavy cavitation was observed above the trailing edge. The scalar transport model predicted periodic growth and decay of the liquid vapor fraction above the trailing edge owing to local variations in

pressure minima. The frequency of this variation was on the order of 300 Hz similar to those observed in the experiments. The discrete bubble model captures the subgrid dynamics of bubbles and also showed cavitation inception occurring above the trailing edge. For low σ_i , rapid variations in bubble sizes were also observed within the shear layer. Sensitivity of the model parameters was investigated in case of the discrete bubble model by varying the initial size of the bubbles and by changing the cavitation index. It was found that bubbles with initial sizes on the order of 50-100 micron tend to cluster in low pressure regions and exhibit rapid growth. By examining the probability distribution functions and average number of bubbles, the inception index of 0.9 agrees well with the experimental data.

ACKNOWLEDGMENT

This work was supported by the Office of Naval Research (ONR) grant number N000140610697. The program manager is Dr. Ki-Han Kim. We thank Prof. Joseph Katz and Dr. Xiaofeng Liu of Johns Hopkins University for the experimental data as well as useful discussions.

REFERENCES

- [1] Liu, X., and Katz, J., 2008. "Cavitation phenomena occurring due to interaction of shear layer vortices with the trailing corner of a two-dimensional open cavity". *Physics of Fluids*, **20**(4).
- [2] Arndt, R., 2002. "Cavitation in vortical flows.". *Annual Review of Fluid Mechanics*, **34**(1), pp. 143–175.
- [3] Rood, E., 1991. "Review: Mechanisms of cavitation inception". *Journal of Fluids Engineering*, **113**(2), pp. 163–175.
- [4] Johnson, V., and Hsieh, T., 1966. "The influence of the trajectories of gas nuclei on cavitation inception". In Sixth Symposium on Naval Hydrodynamics, pp. 163–179.
- [5] Hsiao, C., and Chahine, G., 2008. "Numerical study of cavitation inception due to vortex/vortex interaction in a ducted propulsor". *Journal of Ship Research*, **52**(2), pp. 114–123.
- [6] Hsiao, C., Jain, A., and Chahine, G., 2006. "Effect of Gas Diffusion on Bubble Entrainment and Dynamics around a Propeller". In Proceedings of 24th Symposium on Naval Hydrodynamics, Rome Italy, Vol. 26.
- [7] De Chizelle, Y. K., Ceccio, S. L., and Brennen, C. E., 1995. "Observations and scaling of travelling bubble cavitation". *Journal of Fluid Mechanics Digital Archive*, **293**(-1), pp. 99–126.
- [8] Cerutti, S., Knio, O., and Katz, J., 2000. "Numerical study of cavitation inception in the near field of an axisymmetric jet at high Reynolds number". *Physics of Fluids*, **12**, p. 2444.
- [9] Kim, J., Paterson, E., and Stern, F., 2006. "RANS simulation of ducted marine propulsor flow including subvisual

- cavitation and acoustic modeling”. *Journal of Fluids Engineering*, **128**, p. 799.
- [10] Farrell, K., 2003. “Eulerian/Lagrangian analysis for the prediction of cavitation inception”. *Journal of Fluids Engineering*, **125**(1), pp. 46–52.
- [11] Alehossein, H., and Qin, Z., 2007. “Numerical analysis of Rayleigh–Plesset equation for cavitating water jets”. *Int. J. Numer. Meth. Engng*, **72**, pp. 780–807.
- [12] Wienken, W., Stiller, J., and Keller, A., 2006. “A method to predict cavitation inception using large-eddy simulation and its application to the flow past a square cylinder”. *Journal of Fluids Engineering*, **128**, p. 316.
- [13] Germano, M., Piomelli, U., Moin, P., and Cabot, W., 1991. “A dynamic subgrid-scale eddy viscosity model”. *Physics of Fluids A: Fluid Dynamics*, **3**, p. 1760.
- [14] Merkle, C. L., Feng, J., and Buelow, P., 1998. “Computational modeling of the dynamics of sheet cavitation”. In Proceedings of the 3rd International Symposium on Cavitation (CAV ’98), Grenoble, France.
- [15] Senocak, I., and Shyy, W., 2004. “Interfacial dynamics-based modelling of turbulent cavitating flows, Part-1: Model development and steady-state computations”. *International Journal for Numerical Methods in Fluids*, **44**, pp. 975–995.
- [16] Hsiao, C., and Chahine, G., 2002. “Prediction of vortex cavitation inception using coupled spherical and non-spherical models and UnRANS computations”. In Proceedings of 24th Symposium on Naval Hydrodynamics, Fukuoka, Japan.
- [17] Apte, S., Shams, E., and Finn, J., 2009. “A hybrid Lagrangian-Eulerian approach for simulation of bubble dynamics”. In Proceedings of the 7th International Symposium on Cavitation, CAV2009, Ann Arbor, Michigan, USA. (submitted).
- [18] Apte, S., Mahesh, K., and Lundgren, T., 2008. “Accounting for finite-size effects in simulations of disperse particle-laden flows”. *International Journal of Multiphase Flow*, pp. 260–271.
- [19] Brennen, C., 1995. *Cavitation and bubble dynamics*. Oxford University Press, USA.
- [20] Chahine, G., 1994. “Strong interactions bubble/bubble and bubble/flow”. In IUTAM conference on bubble dynamics and interfacial phenomena (ed. JR Blake). Kluwer.
- [21] Darmana, D., Deen, N., and Kuipers, J., 2006. “Parallelization of an Euler–Lagrange model using mixed domain decomposition and a mirror domain technique: Application to dispersed gas–liquid two-phase flow”. *Journal of Computational Physics*, **220**(1), pp. 216–248.
- [22] Singhal, A., Vaidya, N., and Leonard, A., 1997. “Multi-dimensional simulation of cavitating flows using a PDF model for phase change”. In ASME Paper FEDSM97-3272, the 1997 ASME Fluids Engineering Division Summer Meeting.
- [23] Senocak, I., and Shyy, W., 2004. “Interfacial dynamics-based modelling of turbulent cavitating flows, part-2: time-dependent computations”. *International Journal for Numerical Methods in Fluids*, **44**, pp. 997–1016.
- [24] Senocak, I., and Shyy, W., 2002. “Evaluation of Cavitation Models for Navier-Stokes Computations”. *FEDSM2002-31011, Proc. of 2002 ASME Fluids Engineering Division Summer Meeting Montreal, CA*.
- [25] Mahesh, K., Constantinescu, G., and Moin, P., 2004. “A numerical method for large-eddy simulation in complex geometries”. *J. Comput. Phys.*, **197**(1), pp. 215–240.
- [26] Mahesh, K., Constantinescu, G., Apte, S., Iaccarino, G., Ham, F., and Moin, P., 2006. “Large-eddy simulation of reacting turbulent flows in complex geometries”. *J. Applied Mech.*, **73**, p. 374.
- [27] Moin, P., and Apte, S., 2006. “Large-eddy simulation of realistic gas turbine-combustors”. *AIAA Journal*, **44**(4), pp. 698–708.
- [28] Apte, S., Mahesh, K., Moin, P., and Oefelein, J., 2003. “Large-eddy simulation of swirling particle-laden flows in a coaxial-jet combustor”. *International Journal of Multiphase Flow*, **29**(8), pp. 1311–1331.
- [29] Pierce, C., and Moin, P., 1998. “Large eddy simulation of a confined coaxial jet with swirl and heat release”. *AIAA Paper*, **2892**.
- [30] Liu, X., and Katz, J., 2006. “Instantaneous pressure and material acceleration measurements using a four-exposure PIV system”. *Experiments in Fluids*, **41**(2), pp. 227–240.